Available online at www.sciencedirect.com
SCIENCE DIRECT
International Journal of Heat and Fluid Flow 27 (2006) 243–258
International Journal of HEAT AND FLUID FLOW
www.elsevier.com/locate/ijhff

Experimental validation of large eddy simulations of flow and heat transfer in a stationary ribbed duct

Evan A. Sewall, Danesh K. Tafti *, Andrew B. Graham, Karen A. Thole

Mechanical Engineering Department, Virginia Polytechnic Institute and State University, 114-I Randolph Hall, Blacksburg, VA 24061, United States

Received 20 January 2005; accepted 31 August 2005
Available online 23 November 2005

Abstract

Accurate prediction of ribbed duct flow and heat transfer is of importance to the gas turbine industry. The present study comprehensively validates the use of large eddy simulations (LES) for predicting flow and heat transfer with measured flowfield data in a stationary duct with 90° ribs and elucidates on the detailed physics encountered in the developing flow region, the fully developed region, and the 180° bend region. Among the major flow features predicted with accuracy are flow transition at the entrance of the duct; the distribution of mean and turbulent quantities in the developing, fully developed, and 180° bend; the development of secondary flows in the duct cross-section and the 180° bend; and friction and heat transfer augmentation. At the duct inlet, both the computations and experiments show that the peak turbulence intensities reach values as high as 40% in the streamwise and spanwise directions and 32% in the vertical direction, and a comparison of values along the centerline of the developing flow region shows that the mean flow and turbulent quantities do not become fully developed until they reach beyond the seventh rib of the duct. Turbulence intensities in the 180° bend are found to reach values as high as 50%, and local heat transfer comparisons show that the heat transfer augmentation shifts towards the outside wall downstream of the bend with little or no shift upstream. In addition to primary flow effects, secondary flow impingement on the smooth walls is found to develop by the third rib, while it continues to evolve downstream of the sixth rib. In all different aspects, it is found that LES produces the correct physics both qualitatively and quantitatively to within 10–15% of experiments.

Keywords: Duct flow; Ribbed channels; LES

1. Introduction

In an effort to build more powerful and efficient engines, the gas turbine industry has worked to enhance cooling methods to accommodate higher turbine inlet temperatures. Ribbed internal cooling ducts in various configurations are commonly used in modern high temperature gas turbine vanes and blades to enhance the heat transfer coefficient. The flows generated by ribs are dominated by separating and reattaching shear layers with vortex shedding and secondary flows in the cross-section. In addition to this, the effects of rotational Coriolis forces and centrifugal buoyancy effects make the accurate prediction of heat transfer coefficients quite challenging.

Computational expense has limited most applications of CFD to solving the Reynolds averaged Navier–Stokes (RANS) equations and using turbulence models for closure in the equations, but more recently the ability to resolve all but the smallest turbulence scales using large eddy simulations (LES) has become more available. LES calculations can potentially produce more accurate results by modeling only the smallest scales, which tend to be more isotropic, while fully resolving the turbulence at the larger scales. While LES predictions have been published in the literature, they have been limited to either a fully developed

* Corresponding author. Tel.: +1 540 231 9975; fax: +1 540 231 9100.
E-mail addresses: esewall@vt.edu (E.A. Sewall), dtafti@vt.edu (D.K. Tafti), grahamab@standford.edu (A.B. Graham), thole@vt.edu (K.A. Thole).

0142-727X/$ - see front matter © 2005 Elsevier Inc. All rights reserved.
doi:10.1016/j.ijheatfluidflow.2005.08.010

Nomenclature

C_p	specific heat
D_h	hydraulic diameter, characteristic length
ΔL	change in streamwise position between two pressure measurements
Nu	local Nusselt number
$\overline{Nu}$	spatially averaged Nusselt number
P	rib pitch
Pr	Prandtl number ($=\mu C_p/k$)
Re	Reynolds number ($=\bar{u}_{in}D_h/v$)
T	temperature, characteristic temperature for developing flow and 180° bend cases is ($T_s - T_{in}$)
e	rib height
f	Fanning friction factor
k	thermal conductivity
p	non-dimensional pressure
q''	non-dimensional heat flux on duct walls and ribs, characteristic temperature for fully developed case is ($q''D_h/k$)
tke	turbulent kinetic energy described by: tke $= \frac{\left(\overline{u'^2}+\overline{v'^2}+\overline{w'^2}\right)}{2\overline{u_{in}}^2}$
$\vec{u}$	Cartesian velocity vector (u,v,w) or (u_1,u_2,u_3)
$\bar{u}_{in}$	inlet flow velocity/mean bulk flow velocity, characteristic velocity
u	streamwise velocity, non-dimensionalized by the characteristic velocity
v	non-dimensional cross-stream velocity
w	non-dimensional spanwise velocity
$\vec{x}$	physical coordinates (x,y,z) or (x_1,x_2,x_3)
θ	non-dimensional temperature, $\left(\frac{T-T_{in}}{T_s-T_{in}}\right)$
$\vec{\xi}$	computational coordinates (ξ,η,ζ)
μ	dynamic viscosity
v	kinematic viscosity

subscripts

s	surface
in	inlet to calculation domain, also used for the average bulk velocity
0	smooth duct
rms	root mean square; fluctuating quantities non-dimensionalized by the characteristic velocity

assumption or to Reynolds numbers less than 10,000, whereas most gas turbine applications have Reynolds numbers greater than 10,000.

In this paper, LES results are validated against experiments at a Reynolds number of 20,000. Three LES calculations in a stationary duct are presented in this paper along with laser Doppler velocimeter (LDV) and infrared (IR) camera heat transfer measurements. The paper validates and discusses the flow physics via mean and turbulent quantities in the developing flow regime, fully developed regime, and flow in a 180° bend.

1.1. Review of relevant studies

Heat transfer experiments have been presented detailing measurements in ducts similar to those in all three regions of the present study, including developing flow (Han and Park, 1988; Liou and Hwang, 1992a; Wagner et al., 1992; Wang et al., 2001; Chang and Morris, 2003), fully developed flow (Han, 1984; Liou and Hwang, 1992b; Baughn and Yan, 1992; Fann et al., 1994; Park et al., 1998; Mochizuki et al., 1999; Ekkad et al., 2000; Chen et al., 2000; Islam et al., 2002; Rau et al., 1998), and flow in the 180° bend region (Han et al., 1988). In addition, flow measurements in the fully developed region have been obtained using LDV measurements (Rau et al., 1998; Sato et al., 1989; Liou et al., 1993a; Graham et al., 2004) and hot-wire anemometer measurements (Hirota et al., 1992). These have been combined with measurements in many other geometric configurations and flow conditions to provide a wide database of experimental data for ribbed ducts.

Computational studies have also been used extensively in studying the flow and heat transfer effects in ribbed ducts. The advantage of being able to study both the flow and heat transfer in the entire flowfield is worth the effort required to simulate ribbed duct flows, but the current practice of studying ribbed ducts relies heavily on RANS turbulence modeling, which typically does not have the repeatability and accuracy required of a prediction tool across the wide range of physical phenomena encountered in internal cooling flows. Despite these shortcomings, however, calculations using turbulence models can still produce fairly good results and are used widely because of the speed with which results can be obtained.

Studies using the standard k–ε turbulence model have demonstrated the failure of turbulence modeling that does not account for anisotropy in the turbulence when simulating ribbed duct flows. Large portions of the calculations were predicted incorrectly (Durst et al., 1988; Liou et al., 1990; Acharya et al., 1993; Prakash and Zerkle, 1995; Zhao and Tao, 1997; Ooi et al., 2002). Two of these studies identified the most significant problems as the failure of the turbulence models to correctly predict the Reynolds stresses in the regions with high anisotropy, namely the separated flow and large recirculation zone downstream of the ribs (Liou et al., 1990; Acharya et al., 1993). A study by Ooi et al. (2002) compared a standard k–ε model with the one-equation Spalart–Allmaras (SA) model and the v^2–f

model. The v^2–f model produced the best results (the others performed poorly), but it still failed to reproduce the secondary flows with accuracy, which have a significant impact on the heat transfer. Two two-dimensional calculations by Liou et al. (1992, 1993b) used a k–ε–A model, which is a standard k–ε model coupled with an Algebraic Stress Model (ASM), and were able to account for the anisotropy of turbulence.

Calculations using a number of different turbulence models by Arts et al. (1997) showed that a three dimensional k–l model (similar to k–ε) was not sufficient in predicting the secondary flows and an ASM was required. A comparison between an eddy-viscosity model (EVM) and an ASM reported that the average heat transfer on the side wall (which is most affected by secondary flows) was predicted to within 5%, but contours of the regions showed predictions that were completely different from what the experimental measurements showed (Saidi and Sundén, 2001). Jia et al. (2002) employed an ASM and showed that the vertical rms value was overpredicted near the wall, but centerline heat transfer augmentation was still predicted well. A comparison between effective viscosity models and differential second-moment closure (DSM) models in two dimensions by Iacovides and Raisee (2001) showed that, even though the DSM model could account for the anisotropic turbulence, it could not completely reproduce the heat transfer in all cases. A study comparing several k–ε models and k–ω models with a Reynolds Stress Model (RSM) with enhanced wall treatment showed good agreement between the RSM results and experiments in predicting mean flow and smooth side wall heat transfer with some differences in predicting ribbed wall heat transfer (Sleiti and Kapat, 2004).

Much work has been done in comparing turbulence models in ducts with ribs angled at 45° in addition to the studies mentioned so far, which have all focused on ribs angled at 90° to the flow. Because of the presence of large pressure-driven secondary flows and a completely different flowfield, modeling turbulent flow in ducts with 45° ribs presents different challenges and is not discussed in this paper (Bonhoff et al., 1997; Shih et al., 1998; Bonhoff et al., 1999; Astarita et al., 2002; Astarita and Cardone, 2003; Lin et al., 2001; Jang et al., 2001; Al-Qahtani et al., 2002a,b; Iacovides et al., 2003).

An LES calculation of a stationary ribbed duct was reported by Murata and Mochizuki, but the Reynolds number was low and no comparisons with experiments were provided to clarify the accuracy (Murata and Mochizuki, 2001). Watanabe and Takahashi (2002) presented an LES calculation of a fully developed stationary ribbed duct at $Re = 117{,}000$, and results showed excellent agreement with mean velocity profiles and good agreement with heat transfer measurements. A study comparing unsteady RANS (URANS) calculations to LES found both calculations to be within 20% of experiments (Saha and Acharya, 2003). Excellent comparisons between LES calculations and experiments have been shown in fully developed stationary ducts by Tafti (2005), in fully developed rotating ducts by Abdel-Wahab and Tafti (2004a), in fully developed stationary ducts with 45° ribs by Abdel-Wahab and Tafti (2004b), and in developing flow in stationary and rotating ducts by Sewall and Tafti (2004a,b).

1.2. Objectives

The objective of this paper is to compare the results of LES calculations with experiments to elucidate on the flow physics, demonstrate the accuracy of the calculations and to identify shortcomings if any. While in many previous studies (Prakash and Zerkle, 1995; Zhao and Tao, 1997; Bonhoff et al., 1997; Lin et al., 2001; Jang et al., 2001; Al-Qahtani et al., 2002a,b; Murata and Mochizuki, 2001; Saha and Acharya, 2003) comparisons are mostly limited to heat transfer measurements in the fully developed region by using *similar* experiments from the literature, the present study provides a broad range of hydrodynamic (mean and turbulent) and heat transfer comparisons in the developing flow, fully developed and 180° bend domains with both LDV and IR camera experiments performed by the authors on exactly the same geometry, and these are coupled with additional experiments found in the literature. In all calculations, the square duct is stationary with square in-line ribs on two opposing walls. The ribs have a rib height-to-hydraulic diameter ratio (e/D_h) of 0.1 and a rib pitch-to-rib height ratio (P/e) of 10, and the channel aspect ratio is 1:1. The bend region has square corners and a dividing wall that is $1/2D_h$ thick, and the length from the end of the divider to the back wall is $1D_h$. There are no ribs in the bend. The channel is stationary and the flow Reynolds number based on bulk velocity and hydraulic diameter is 20,000.

2. Experimental apparatus and measurement techniques

The data included in this paper, flow field and pressure drop measurements, were made in a ribbed channel facility, shown in Fig. 1. A detailed description is given in Graham et al. (2004), so only the essential details are provided here. The test section includes a straight section that is approximately 3.53 m ($24D_h$) in length, a sharp bend region, and a return flow region of approximately 1.5 m ($10D_h$) in length. Ribs are attached to the bottom and top walls of the channel in an in-line arrangement. The ribs are square in cross-section with a rib height of 1.49 cm ($e/D_h = 0.1$). The loca-

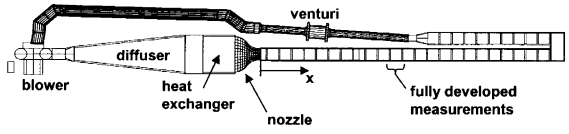

Fig. 1. The closed loop test facility includes a 2 hp blower, a plenum with a heat exchanger, $1\frac{1}{2}$ ribbed channels, and a venturi flow meter downstream of the return leg.

tion of the first rib is placed at 6.7 cm (0.45 rib pitches), or 4.5 rib heights, downstream of the contraction exit.

Prior to making the LDV measurements, pressure drop measurements were completed for a range of conditions to allow friction factors to be compared with the literature and calculations. To determine the increased frictional losses resulting from the ribs, pressure taps were installed along the entire channel length of the smooth side wall and were spaced 14.9 cm apart and located directly between the ribs. Both average (over many ribs) friction factors as well as local (across one rib) friction factors were calculated. The average friction factors included all of the ribs extending from the fourth rib to the 23rd rib. The normalizing relation for the friction factors was (Incropera and DeWitt, 2002)

$$f_0 = 0.046Re^{-0.2} \tag{1}$$

Flowfield measurements for this study included the mean and the corresponding root-mean-square (rms) velocities. A two-component back-scatter fiber optic LDV system was used in this study that consisted of a 5 W laser and a TSI model 9201 Colorburst beam separator. Velocity data was processed using TSI model IFA 755 Digital Burst Correlator controlled using TSI's FIND software. The LDV was positioned on the side of the test channel to capture the streamwise (u) and vertical (v) components of the velocity. To capture the smallest control volume, a 450 mm focusing lens was used in conjunction with a beam expander. The probe volume length and diameter were 0.32 mm and 44 μm, respectively. The LDV probe was tilted at 10° to allow for measurements very near the surface. For the LDV measurements, each mean and rms velocity was averaged between 10,000 and 20,000 points, which took nominally 20 s to acquire. All measurements were corrected for bias errors using the well accepted time weighted average correction scheme. The flow was seeded using olive oil having a nominal particle diameter of 1 μm.

An infrared camera was used to measure the heat transfer augmentation on one ribbed wall section and one smooth side wall section in the fully developed region of the duct. Each picture covered an area that was approximately 14.9 cm by 14.9 cm with the area being divided into 360 by 240 pixel locations. At each viewing location five images were averaged, with each image being averaged over 16 frames, providing a total of 80 data points averaged at each pixel location. Calibration of the infrared camera was made using three thermocouples embedded in each wall examined. Thermocouples were also used to monitor the bulk fluid temperature. A uniform heat flux boundary condition was imposed on the walls by a series of foil resistance heaters mounted to the walls and ribs. Foil heaters were applied to all surfaces of the ribs on a separate electrical circuit to apply the same heat flux boundary condition as that on the walls. The voltage across a precision resistor in series with the heaters and the voltage across the heaters were used to obtain the heat flux on the walls. The heat transfer was obtained by calculating the Nusselt number with the following equation:

$$Nu = \frac{q''}{(T_s - T_b)} \cdot \frac{D_h}{k} \tag{2}$$

where T_s is the surface temperature measured by the infrared camera and T_b is the bulk fluid temperature interpolated from a measured inlet temperature to the measurement location by an energy balance. The heat transfer measurements were normalized by the Dittus–Boelter correlation (Incropera and DeWitt, 2002)

$$Nu_0 = 0.023 \cdot Re^{0.8} \cdot Pr^{0.4} \tag{3}$$

Overall uncertainties were calculated for the friction factors and flow field measurements according to the partial derivative method described by Moffat (1988). The total uncertainty of all measurements was calculated as the root of the sum of the squares of the precision uncertainty and the bias uncertainty. The precision uncertainty was based on a 95% confidence interval. The estimate of bias uncertainties for the mean velocities was 1%. The precision uncertainty for the streamwise rms velocities was 2.6%. For the friction factors, the uncertainty was calculated to be 6%. For the heat transfer measurements, the uncertainty at a Nusselt number of 85 is 6.9% and at a Nusselt number of 165, the uncertainty is 12.9%.

3. Computational models and governing equations

The three calculation domains used in this study are shown in Fig. 2. In the developing flow region (Fig. 2(a)), the flow and heat transfer are studied in the first eight ribs of the duct, with the ninth rib and extension region downstream providing the buffer region for the application of the outflow boundary condition. At the inlet, a laminar plug flow velocity profile is used, which is an approximation of the inlet conditions used in previous experimental developing flow studies (Han and Park, 1988; Liou and Hwang, 1992a), in which flow was directed from a plenum into the test section to produce inlet conditions with low turbulence. The governing flow equations are non-dimensionalized by a characteristic length scale, given by the channel hydraulic diameter (D_h), a characteristic velocity scale, given by the channel bulk velocity ($\overline{u}_{in}$), and a characteristic temperature scale, given by the wall temperature difference ($T_s - T_{in}$).

In the fully developed flow model (Fig. 2(b)), a periodically repeating spatial unit with one rib is simulated. The governing flow equations are non-dimensionalized by a characteristic length scale, given by the hydraulic diameter of the channel (D_h), a characteristic velocity scale, given by the friction velocity ($u_\tau = \sqrt{\Delta P_x/\rho}$), and a characteristic temperature scale, given by the non-dimensional heat flux ($\frac{q''D_h}{k}$). The assumed periodicity of the domain in the streamwise or x-direction requires that the mean gradients of pressure and temperature be isolated from the fluctuating periodic component as follows:

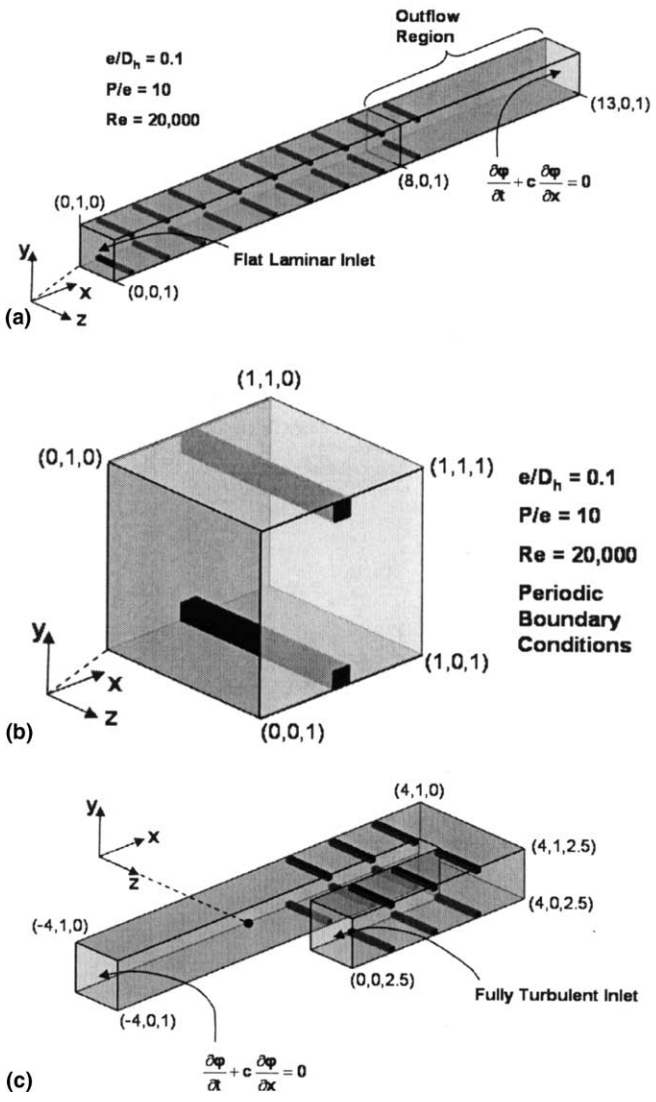

Fig. 2. The calculations in this project include the (a) developing flow, (b) fully developed flow, and (c) a 180° bend region.

$$P(\vec{x},t) = P_{\text{in}} - \beta x + p(\vec{x},t) \tag{4}$$

$$T(\vec{x},t) = T_{\text{in}} + \gamma x + \theta(\vec{x},t) \tag{5}$$

The calculation of the 180° bend consists of three ribs upstream of the bend and three ribs downstream and is shown in Fig. 2(c). Inlet time-dependent turbulent boundary conditions are generated by using a series of frames extracted from the developing flow calculation downstream of the fifth rib and applied to the 180° bend at a location of $0.925D_{\text{h}}$ upstream of the midpoint of the first rib. The frames were extracted over a total time of 1/4 time unit, and the final 4% were linearly interpolated between the end and beginning states to provide continuity when the series was repeated. The governing equations for this calculation are non-dimensionalized in the same way as those for the developing flow calculations.

The equations governing the flow are the time-dependent Navier–Stokes equations in transformed coordinates. They are described in Sewall and Tafti (2004a) for the developing flow and 180° bend calculations and Tafti (2005) for the fully developed calculation. The Cartesian velocities are non-dimensionalized by the bulk velocity, and the turbulence quantities are non-dimensionalized by the bulk velocity squared. The dynamic Smagorinsky subgrid scale model is used to model the smallest scales. Details of the model are given in Tafti (2005). The Smagorinsky constant is calculated dynamically via the dynamic subgrid stress model (Germano et al., 1991), and the final version of the constant is found with the least-squares minimization procedure of Lilly (1992).

The governing equations are discretized with a conservative finite-volume formulation using a second-order central difference scheme on a non-staggered grid topology. The Cartesian velocities and pressure are calculated and stored at the cell center, whereas contravariant fluxes are calculated and stored at the cell faces. For the time integration of the discretized continuity and momentum equations, a projection method is used. The temporal advancement is performed in two steps, a predictor step, which calculates an intermediate velocity field, and a corrector step, which calculates the updated velocity at the new time step by satisfying discrete continuity. Details about the algorithm, functionality, and capabilities can be found in Tafti (2001).

The computer program GenIDLEST (Generalized Incompressible Direct and Large Eddy Simulations of Turbulence) used for these simulations has been applied to fully developed flow and heat transfer in a ribbed duct geometry similar to the one used in this study (Tafti, 2005), with rotation and buoyancy effects (Abdel-Wahab and Tafti, 2004a), and in a channel with 45° ribs (Abdel-Wahab and Tafti, 2004b). In all of these cases it has been consistently established through comparison with experiments that predictions of mean flow, turbulent quantities, and heat transfer, are accurate to within ±10% of experiments and in some cases within experimental uncertainty.

4. Computational details

In the developing flow region and 180° bend region, each rib pitch has a similar grid distribution as the 96^3 resolution periodic channel presented in Tafti (2005). A grid independence study between a periodic channel with 96^3 and 128^3 grid points showed no significant differences in the prediction of heat transfer and friction between the low and high resolution cases when the dynamic Smagorinsky subgrid scale model is used. Slightly higher channel centerline turbulence indicated that the 96^3 grid might be too coarse in the channel center, but this had no apparent effect on heat transfer or friction at the walls, which are much more dependent on near wall turbulence. Both meshes predicted the local and mean heat transfer augmentations within experimental uncertainty on the ribbed wall and smooth walls. For this reason and because of the large size of the developing flow domain, the 96^3 mesh is used for

each rib. The total mesh size for the developing flow calculation is 8.85×10^6 computational cells and for the 180° bend calculation is 8.40×10^6 cells. In the fully developed region the higher resolution calculation with 128^3 cells is reported, having a total of 2.10×10^6 cells.

The non-dimensional time step (non-dimensionalized by the length scale divided by the characteristic velocity) in the calculations is set to 5×10^{-5}. The diffusion terms are treated implicitly, and the average L_1 residual norm of global mass balance is converged to 1×10^{-8}, while the momentum equations are converged to 1×10^{-7}. The calculations utilized 160, 32, and 152 processors of an IA-64 Itanium Linux cluster for the developing, fully developed, and 180° bend calculations, respectively. Each time step took about 0.5 μs/grid node of wall clock time.

For the developing flow and 180° bend regions, the calculations were initiated by assuming initial conditions similar to a fully developed channel and integrating in time until the flow reached a statistically stationary state. The time evolution of bulk quantities such as Nusselt number, wall heat flux, friction drag losses, and form drag losses were observed until all values reached a uniform state. Once stationary conditions were established, sampling to obtain mean and turbulent quantities was carried out for approximately 10 time units in each calculation. Initial mean quantities were obtained by sampling over one time unit before obtaining turbulent statistical quantities. In the developing and fully developed sections, the sampling time was quadrupled by using the bi-directional y–z symmetry of the duct and presenting the averaged and turbulent quantities for 1/4th of the duct cross-section. In the 180° bend calculation, the x–z symmetry plane was used to double the sampling time and results are presented for one half of the duct.

5. Results

5.1. Distributions of mean flow and turbulent quantities in developing and fully developed regions

Calculation details in the developing and fully developed domains have been published elsewhere (Tafti, 2005; Sewall and Tafti, 2004a), but the focus of this section is to quantify the prediction accuracy of the calculations with a series of comparisons with experiments and other calculations. The prediction accuracy of the LES calculations compared to that of standard RANS calculations is of interest to help qualify the tradeoff between the industry standard RANS calculations and the more expensive but less empirical LES calculations.

Fig. 3 shows the measured and predicted centerline streamwise velocity and streamwise, vertical, and spanwise (predicted only) turbulent quantities. At the entrance, a spike in the streamwise velocity shows the sudden acceleration of the flow due to the contraction forced by the first ribs past the entrance to the duct. The acceleration is followed by a region of deceleration resulting in a pressure

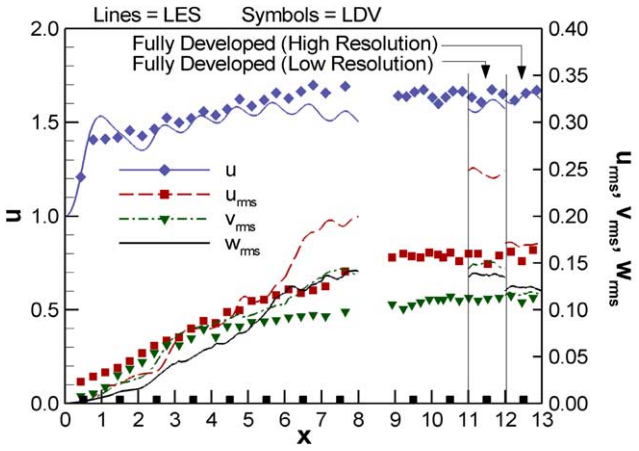

Fig. 3. The streamwise velocity and turbulence quantities in all three directions in the channel center show the longer development length compared to that measured near the ribbed walls, which is typically reported as three to four ribs (symbols = measurements; solid lines = predictions).

recovery. The less dramatic effect in the experiments is attributed to the presence of turbulence at the inlet (2–3%). The measured centerline velocity increases until flow reaches the seventh rib, after which it settles down into a periodic pattern. The computations, on the other hand, settle into a periodic pattern after the fourth rib. The predicted flow transitions to turbulence immediately after the first rib as the separated shear layers on the ribs develop three-dimensional instabilities. The turbulence generated near the ribbed walls diffuses to the center of the channel as flow moves into the duct with a steady near-linear increase in turbulence intensities up to about the eighth rib. The figure shows that increasing the calculation resolution to 128^3 from 96^3 improves the centerline velocity prediction. The overprediction of streamwise turbulence intensity at the center of the channel is also suspected to be a caused by the coarse-mesh resolution. The results are consistent with a grid dependence study of fully developed calculations reported in Tafti (2005). They showed that at low resolution (96^3) higher turbulence levels are predicted at the center of the channel than at higher resolution (128^3). The initial underprediction of the turbulence intensities near the inlet is a result of the preexisting turbulence in the experiments, whereas no turbulence was specified at the inlet of the calculation. In the fully developed region, the turbulence quantities are approximately 16%, 11%, and 12% for u_{rms}, v_{rms}, and w_{rms}, respectively. These are similar to the measured values of 14% and 11% for u_{rms} and v_{rms} as reported by Rau et al. (1998). Overall, the comparison between the measured and predicted quantities is excellent between the high resolution fully developed calculations and measurements, and somewhat good agreement is seen between the low resolution developing flow and fully developed calculations. It is noted that the overprediction of turbulence is only present at the center of the channel because of the coarse mesh and does not influence the

prediction of the heat transfer coefficient on the ribbed wall which is much more dependent on near wall turbulence intensities. This same effect was observed in an earlier grid dependence study (Tafti, 2005).

Mean and turbulent profiles in the symmetry plane midway between pairs of ribs in the developing flow region are shown in Fig. 4. The negative value in the streamwise velocity profile (Fig. 4(a)) near the entrance shows the presence of the large recirculation region stretching past the midpoint between the first two ribs, while the other profiles show no evidence of recirculation, indicating that reattachment has occurred before the midpoint. In Fig. 4(b), the streamwise turbulence profiles are shown. Downstream of the first rib, the rms value peaks at 40% in the shear layer above the rib with values as high as 22% near the ribbed wall. At the channel center, the calculations predict a value of 1.2%, while the experiments show 5.8%. As the flow evolves in the duct, the maximum is found in the shear layer at rib height ($y = 0.1$) and has a value of 32%, 20% less than the peak in the profile downstream of Rib 1. In the channel center, the computations show values of 2–6%, while the experiments show 9–10%. The difference throughout the first four ribs is approximately 4%. Fig. 4(c) shows the vertical, or cross-stream, fluctuations. Similar to the streamwise turbulence, the peak after the first rib (32%) also flattens out as the turbulence diffuses towards the center of the duct. The centerline experimental cross-stream rms values reach about 8%. Finally, Fig. 4(d) shows the calculated spanwise fluctuations (LDV measurements were not taken of w_{rms}). The high magnitudes downstream of Rib 1 (peak of 40%) show that the flow immediately becomes three-dimensional. The spanwise turbulence continues to remain high in the shear layers as the flow develops but also has a well-defined peak near 25% in the boundary layer on the ribbed wall. Turbulence develops rapidly near the ribbed wall and reaches near-fully-developed values by the third or fourth rib.

This rapid development of turbulence quantities near the ribbed wall is highlighted in Fig. 5, which shows spanwise fluctuations (w_{rms}) in a plane through the mid-height of the ribs ($y = 0.05$). Spanwise turbulent fluctuations first develop upstream of the first rib in the region where the inlet flow impinges on the rib. The rib-wall junction is home to highly unsteady secondary vortices, and the development of w_{rms} in this region is directly attributed to these structures. This region subsequently exhibits high intensities at downstream ribs. Downstream of the first rib, the spanwise fluctuations exhibit values as high as 35% in the separated shear layer. Downstream of the second rib, the maximum value in the shear layer decreases to about 25%. The distribution of w_{rms} in this plane is fairly well established as early as the second rib and quickly settles down into a periodic pattern with small variations.

Fig. 6(a) shows the variation of streamwise velocity in the symmetry plane of the duct in the fully developed region. The predictions show the reattachment point of the main recirculation zone to be located about four rib

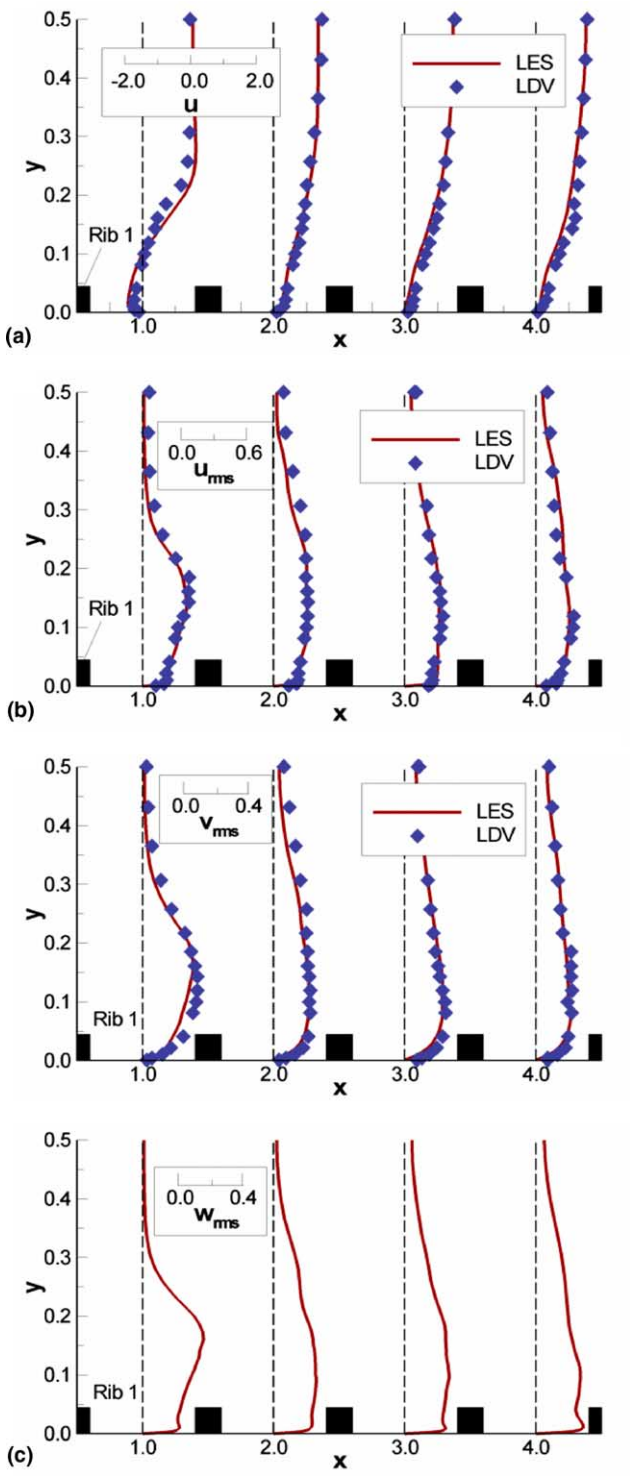

Fig. 4. Vertical profiles of (a) streamwise velocity, (b) streamwise rms, (c) vertical rms, and (d) spanwise rms between ribs downstream of the entrance show the effect of flow development on the velocity and turbulence profiles.

heights downstream of the rib ($x = 0.95$) and the experiments of Rau et al. (1998) reach a similar conclusion ($x = 0.950$–0.975). The LDV measurements show reattachment to be somewhere between $x = 0.83$ and $x = 1.00$, which is in line with Rau et al. and the predictions. These

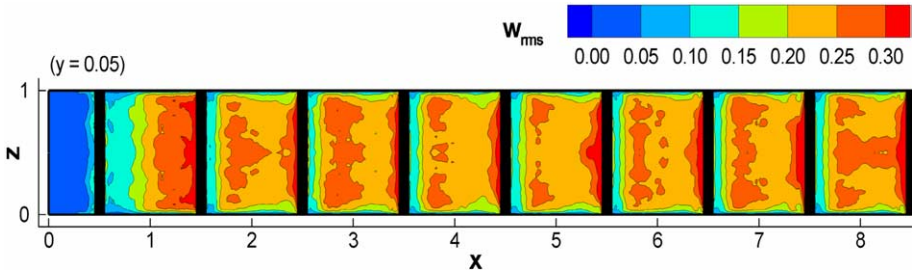

Fig. 5. Spanwise fluctuations in a plane passing through the mid-height of the ribs show a rapid increase and attainment of near-fully-developed conditions in near wall turbulence.

results are consistent with a particle image velocimetry (PIV) study of turbulent water flow through a ribbed duct, which found that flow reattachment remains constant at about four rib heights ($x \approx 0.95$) after the Reynolds number increases past a critical value of 15,000 (Islam et al., 2002).

In Fig. 6(b)–(d), the evolution of turbulence along one rib pitch in the symmetry plane is shown. The streamwise peak value of nearly 50% is observed in the shear layer on top of the rib, which decays to a maximum of near 30% downstream of the rib. Near the ribbed wall in the boundary layer, maximum values close to 20% are sustained over most of the pitch. In contrast to u_{rms}, the maximum value of v_{rms} maintains a maximum value of approximately 25% over the full pitch. Finally, the calculated values of w_{rms} in the symmetry plane are shown in Fig. 6(d) (LDV measurements were not taken of w_{rms}). The spanwise fluctuations look similar to the streamwise fluctuations near the wall, with values of approximately 20% in the boundary layer. All three turbulent fluctuations that are generated in the separated shear layer are transported to the vicinity of the wall as the shear layer reattaches and in the process augment near wall turbulence and heat transfer.

5.2. Mean flow and turbulent quantities in 180° bend

The flow entering the bend in a ribbed duct is characterized by high turbulent intensities (between 35% and 50% in shear layers) and a mean velocity profile which is considerably more non-uniform in the cross-section (maximum of 1.6–1.7 times the bulk velocity versus 1.1–1.2 for a smooth duct). Fig. 7 shows the basic flow features of the bend in a symmetry plane that lies directly between the ribbed walls. The streamwise flow begins to be affected by the turning region about $1D_h$ upstream of the last rib. The flow accelerates considerably on the inside of the turn, forming a strong shear layer at the upstream edge of the bend. Since the bulk of the flow is pushed towards the downstream side of the bend, a large recirculation region forms at the upstream outer corner. Similarly, a smaller recirculation zone forms in the downstream outer corner. The shear layer which forms at the upstream edge of the bend separates from the inside of the bend and forms a recirculation zone at the tip of the dividing wall. The rest of the flow going into the bend impinges on the back wall as it is redirected. Coming out of the bend, the flow once again impinges on the outer wall of the downstream leg. In doing so, the separated shear layer is not allowed to follow its natural trajectory but is pushed back and forced to attach at the downstream inner corner of the bend.

Fig. 8 shows a series of LDV profiles at different y-locations and their comparisons with LES data in the midplane of the bend. A negative velocity represents flow in the streamwise direction, while a positive velocity represents flow reversal. At all y-locations, the velocity in the outer part of the bend ($x = 3.6$–4) is quite uniform with a magnitude of approximately 1.5 times the bulk velocity. However, at the inside of the bend, the streamwise velocity steadily decreases (smaller w values) as y increases with a reversal in the flow direction occurring between $y = 0.27$ and $y = 0.44$. The profile at $y = 0.27$ shows a velocity of nearly zero, indicating that the recirculation zone occupies about 40% of the height of the duct. The size of the recirculating flow is predicted exactly, as shown by the location of zero velocity between the streamwise and recirculating flows. In Fig. 8(b), the streamwise fluctuations (w_{rms}) are plotted at the same locations. Streamwise rms values reach a maximum of 50% at the inside of the bend, while the minimum turbulence is about 20%. The profiles show that the turbulence actually decreases at the center of the duct, in the middle of the recirculation bubble, while the peak value is found at the edge of the recirculation zone, which coincides with the trajectory of the shear layer from the bend.

5.3. Secondary flow in developing and fully developed regions

An important aspect of duct flows is the presence of secondary cross-sectional flows, which have a large impact on heat transfer augmentation on the side walls. In 90° ribbed ducts, these flows are driven by the periodic flow disturbance caused by the ribs and the junction flow where the rib meets the side wall (Tafti, 2005). The combined effect of the rib and the side walls induces weak secondary flows in the cross-section of the duct. In the vicinity of the rib-side wall junction, strong localized unsteady vortical structures are generated. As these vortical structures convect over the rib they draw fluid in towards the side wall. This

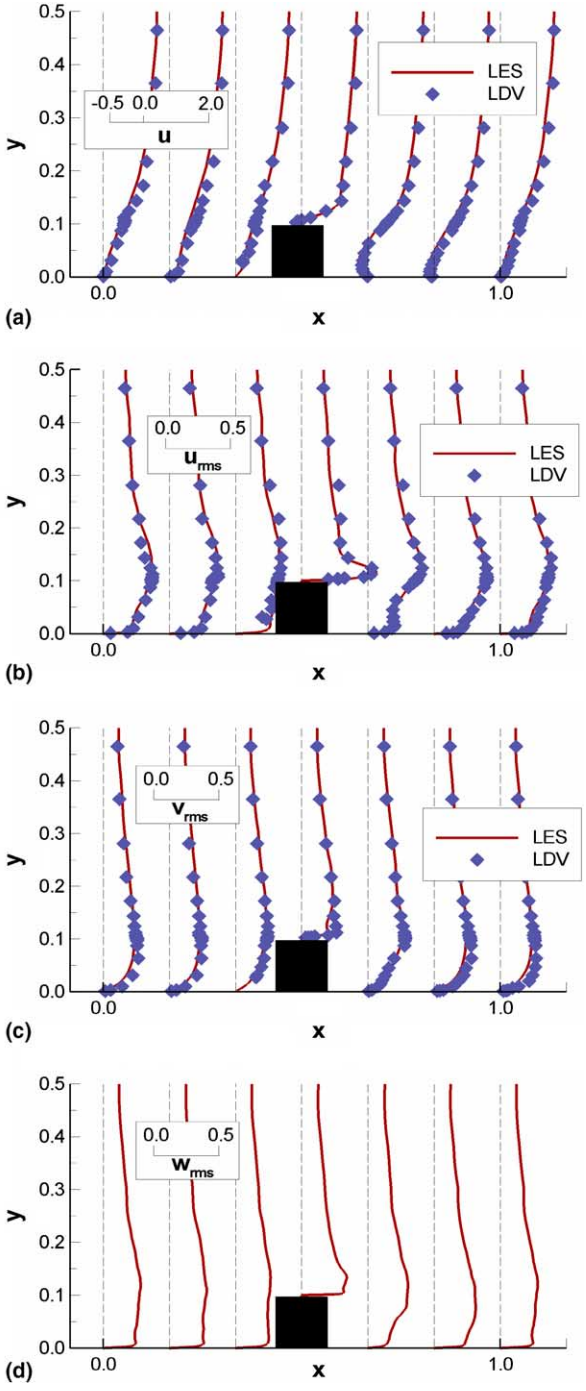

Fig. 6. Measurements of the (a) streamwise velocity, (b) streamwise fluctuations, (c) vertical fluctuations, and (d) spanwise fluctuations in the center plane show the peak values of all quantities near the ribs and their effects on the rest of the duct.

effect, together with the vertical velocity induced by rib blockage, produces impingement and upward flow along the side walls in the vicinity of the ribs. Fig. 9(b) illustrates this effect in the cross-sectional quadrant, showing the strong inward flow towards the wall, impingement, and a vertical flow towards the center of the channel. Lateral impingement velocities as high as 30% of the mean streamwise velocity are found in this region. Near and before reattachment, the separated shear layer draws fluid in from the center of the duct towards the ribbed wall. Instantaneous data (not shown) indicates that this is once again induced by the rotational velocity of the vortices in the shear layer. This effect is shown in Fig. 9(c). Once the shear layer reattaches, the downward motion towards the ribbed wall is still present but weakens considerably as shown in Fig. 9(a). Except in the immediate vicinity of the rib, the secondary flow is weak. Because of the highly localized nature of the secondary flow, which is mostly driven by instantaneous vorticity at the rib junction with the smooth wall, it is quite challenging to predict with eddy-viscosity RANS models (Prakash and Zerkle, 1995; Ooi et al., 2002; Arts et al., 1997; Saidi and Sundén, 2001). This is unlike the secondary flows experienced in skewed ribs (Bonhoff et al., 1997; Shih et al., 1998; Bonhoff et al., 1999; Astarita et al., 2002; Astarita and Cardone, 2003; Lin et al., 2001; Jang et al., 2001; Al-Qahtani et al., 2002a,b; Iacovides et al., 2003; Abdel-Wahab and Tafti, 2004b), which are much stronger and coherent and are driven by the rib geometry and hence easier to predict.

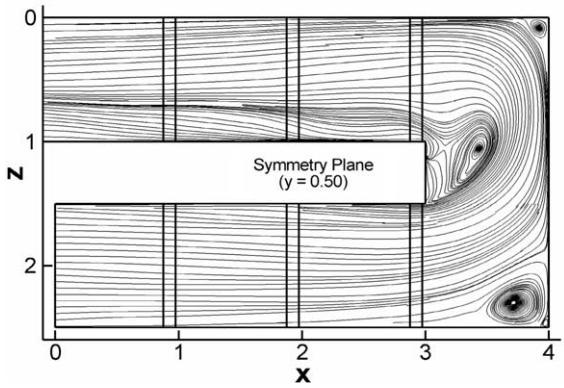

Fig. 7. The main flow features in the 180° bend include recirculation in the upstream corner, separation and reattachment at the end of the divider, and recirculating region in the downstream corner. The bulk fluid impinges on the back wall and the outside wall downstream.

Fig. 10 shows the development of the secondary flow by way of the spanwise mean velocity near the smooth side wall at a location 5% of the channel width away from the wall. The region of strong impingement is established by the third rib, whereas the flow pattern at the center of the duct continues to develop beyond the third rib and reaches a developed state by the sixth rib. A closer look at the secondary flow pattern in the cross-section of the duct (not shown) indicates that the secondary flow pattern evolves even further downstream of the sixth rib. However, the evolution is weak and does not have a major impact on the flow field. Hence, the fully developed secondary flow as shown in Fig. 9 does not differ considerably from that in the developing region after the sixth rib.

5.4. Secondary flow in 180° bend

Fig. 11 shows a plane parallel to the dividing wall and perpendicular to the flow direction at the center of the

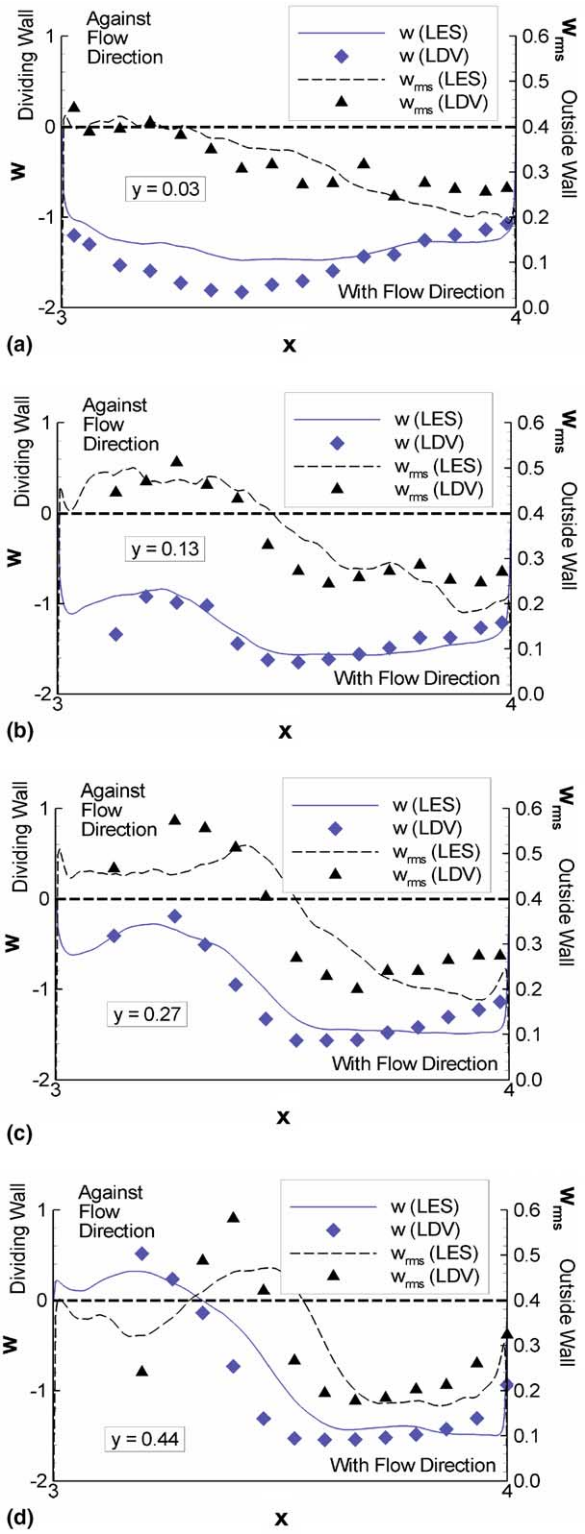

Fig. 8. Profiles of the streamwise velocity and streamwise fluctuations in the bend region, parallel to the dividing wall, show the recirculation region near the dividing wall and the increased turbulence on the inside of the bend region. The maximum streamwise turbulence on this portion of the bend is more than 50%.

180° bend. The flow vectors show a pair of counter-rotating Dean vortices. These are similar to those found in experimental studies of smooth ducts (Liou et al., 1999; Schabacker et al., 1998; Son et al., 2002) and ducts with 45° ribs (Bonhoff et al., 1997; Shih et al., 1998). Similar flow patterns have also been observed in calculations of smooth 180° bends (Lin et al., 2001; Besserman and Tanrikut, 1992; Gu et al., 2002) and bends connecting ducts with 45° angled ribs (Lin et al., 2001; Al-Qahtani et al., 2002a). The impingement of the secondary Dean vortices on the back wall of the bend, at the top and bottom walls towards the outside of the bend, and at the inside of the bend leads to considerable heat transfer enhancement at these locations.

5.5. Friction losses

Table 1 shows a comparison of the fully developed friction factor results from a number of different sources. It is important to note that the friction factor is typically measured by pressure taps along the ribbed or smooth walls, which can potentially produce results that differ from each other, while it is best to report calculated friction factors with area-averaged pressure drops. In Table 1 the area-averaged friction factor augmentation is given, along with local values corresponding to the locations of pressure taps on the ribbed and smooth walls. These values are compared with the experiments from the present study and those of Rau et al. (1998). Because the local pressures are very sensitive to changes in the flow, comparisons between the two measurement types are expected to be close, but not necessarily exactly the same. It has been reported in Rau et al. (1998) and Tafti (2005) that the major contributor to the friction factor is the form loss, which was reported to contribute 85% of the friction factor in Rau et al. (1998) and 91% in Tafti (2005). This high contribution indicates that other flow patterns, such as secondary flows, contribute very little to the overall pressure drop.

Fig. 12 shows the variation of friction factor augmentation calculated from the pressure drops in the 180° bend. The overall area-averaged pressure drops for the groups highlighted in the diagram were obtained from the calculation. The augmentation across Group 1 has a value of 9.8, which is consistent with other reported fully developed friction factors shown earlier in Table 1. The friction factor across Group 2 increases significantly, indicating a strong pressure drop across the rib into the bend. A similar pressure drop across the bend in Group 3 shows the losses occurring between the last rib downstream of the upstream leg of the duct and the first rib in the downstream leg. The most significant friction factor is found in Group 4, where a strong pressure loss occurs across the first rib in the downstream leg. In Group 5, a small negative friction factor indicates the presence of a pressure recovery, where the downstream pressure is higher than the upstream pressure. The recovery is small, indicating that the pressures before and after the second rib in the downstream leg of the duct are equivalent. Two pressure taps were used in the experiments to measure the pressure drop across the bend; their locations are shown in the diagram in Fig. 12. The taps

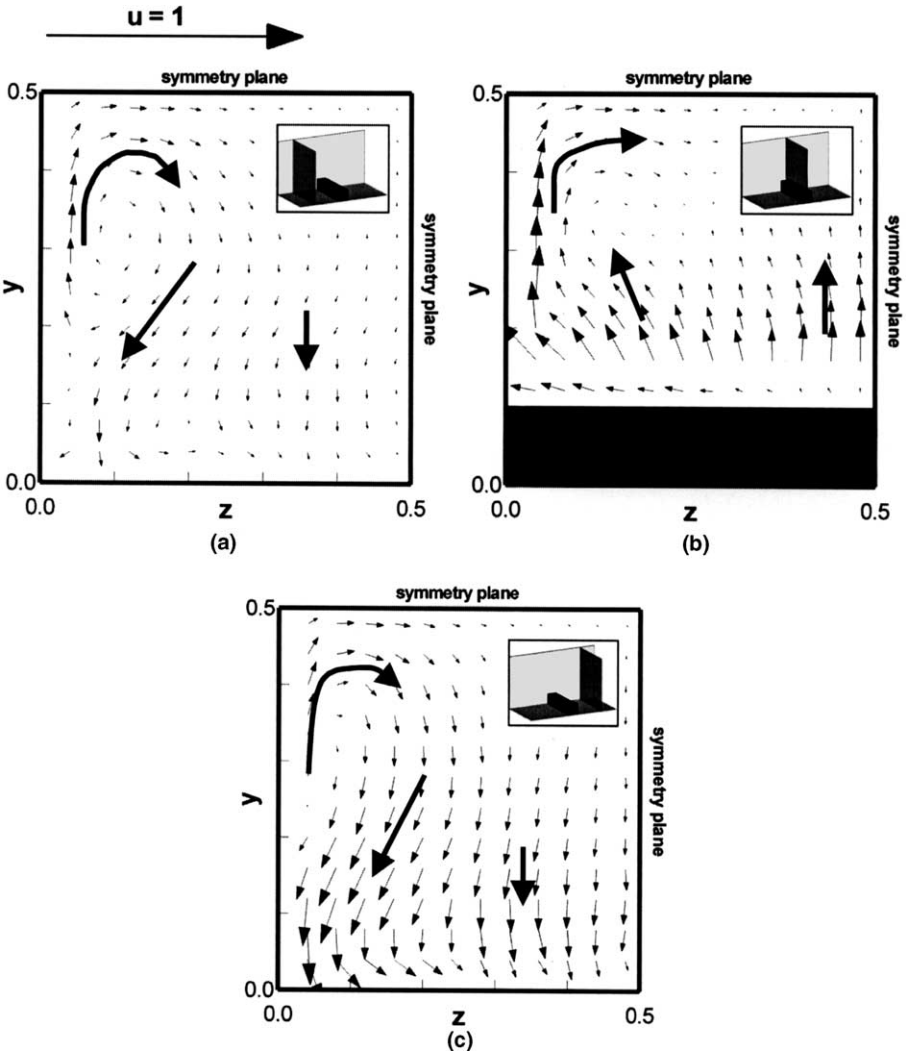

Fig. 9. Cross-stream flow vectors at (a) $x = 0.17$ ($1/3D_h$ upstream of rib), (b) $x = 0.50$ (on top of rib), and (c) $x = 0.83$ ($1/3D_h$ downstream of rib) in 1/4 of the channel cross-section. The extent and strength of the secondary flow in the quadrant changes with axial location.

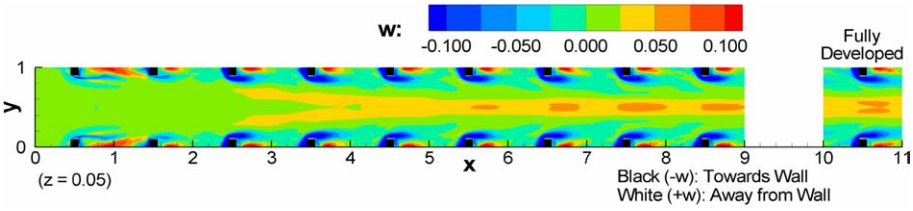

Fig. 10. The spanwise velocity near the smooth side wall shows impingement on the walls above the ribs, along with inward facing flow downstream of the ribs and in the center of the duct. This flow is identical to the fully developed flow after the fifth rib.

were placed along the inside wall, midway between two ribs, at the mid-height of the duct. The friction factor augmentation over the entire 180° bend was found by these pressure measurements to be 22.8. The calculated friction factor, based on area averaged pressures at the same streamwise locations as the pressure taps, has a value of 23.1, which is 1.3% greater than the measured value. Additional pressure taps downstream of the bend show that the friction factor returns to the fully developed value of approximately 10 fairly quickly. Good agreement between the calculations and experiments indicates that the LES calculations are capable of accurately reproducing the measured values of pressure drop.

5.6. Heat transfer augmentation

An accurate determination of the flow physics is paramount for heat transfer predictions, which depend strongly

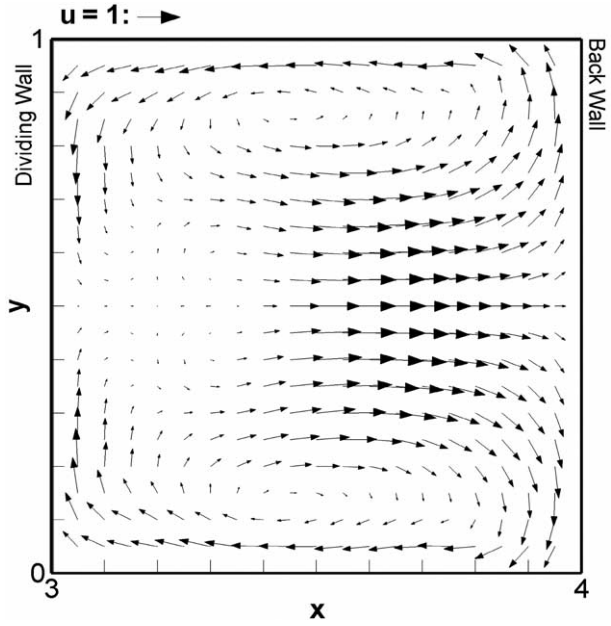

Fig. 11. Vectors in the midplane of the 180° bend show the counter-rotating Dean vortices typically found in flow in a bend. This secondary flow mechanism is responsible for forcing fluid towards the outside wall in the center and up against the inside dividing wall from the top and bottom walls.

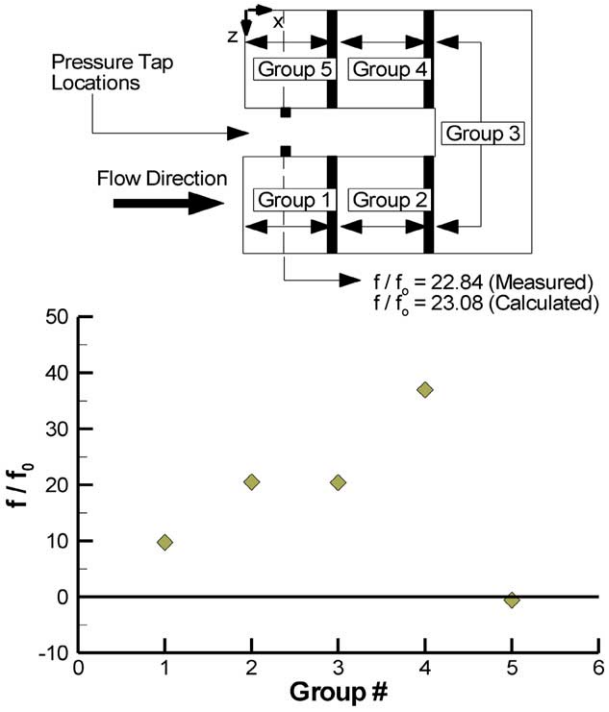

Fig. 12. The friction factor in the 180° bend shows the sharp increase in the pressure drop across the final rib in the upstream leg and the first rib in the downstream leg. A pressure recovery (negative friction factor) is shown immediately downstream of the bend. The calculated and measured friction factors across the bend show excellent agreement between the two values.

Table 1
Fully developed friction factor augmentation

Case	f/f_0			Re
	Area averaged	Smooth wall	Ribbed wall	
Developing Rib 7	9.63	8.82	9.01	20,000
Developing Rib 8	9.84	8.34	9.34	20,000
Fully developed	8.60	–	–	20,000
Experiments	–	8.23	–	20,000
Rau et al. (1998)	–	–	9.50	30,000

on both the mean flow effects and turbulence. In this section, comparisons between calculations and experiments of the heat transfer augmentation in the developing flow, fully developed, and 180° bend regions are presented.

Experimental studies in the developing flow region are far outnumbered by those in the fully developed region, and many experiments in the developing flow region are reported on test sections with ribs smaller than (Han and Park, 1988) or larger than (Liou and Hwang, 1992a) those of the current study. One study, however (Fann et al., 1994), reported results with similar geometric characteristics and a Reynolds number of 20,000. The channel aspect ratio was 1:1, and the ribs were slightly smaller ($e/D_h = 0.08$) and spaced slightly farther apart ($P/e = 11$). These differences are minor, however, and a comparison of four equally-distributed points between the third and fourth ribs (Fig. 13(a)) and the fifth and sixth ribs (Fig. 13(b)) shows very good agreement. The magnitudes of the two comparisons are equal to each other, which further supports the assertion that the ribbed wall heat trans-

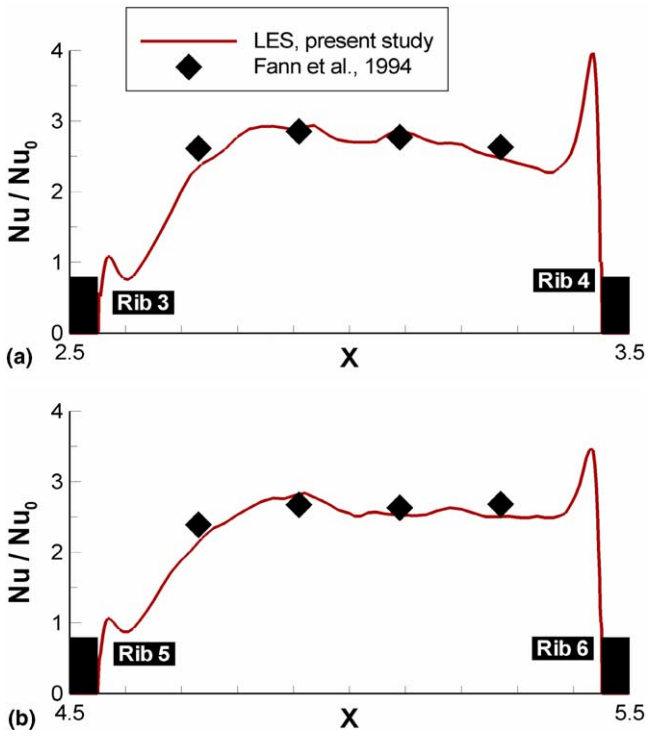

Fig. 13. Comparisons between the local heat transfer measurements of Fann et al. (1994) between (a) Ribs 3 and 4 and (b) Ribs 5 and 6 show the good agreement between the calculations and experiments in the developing flow region.

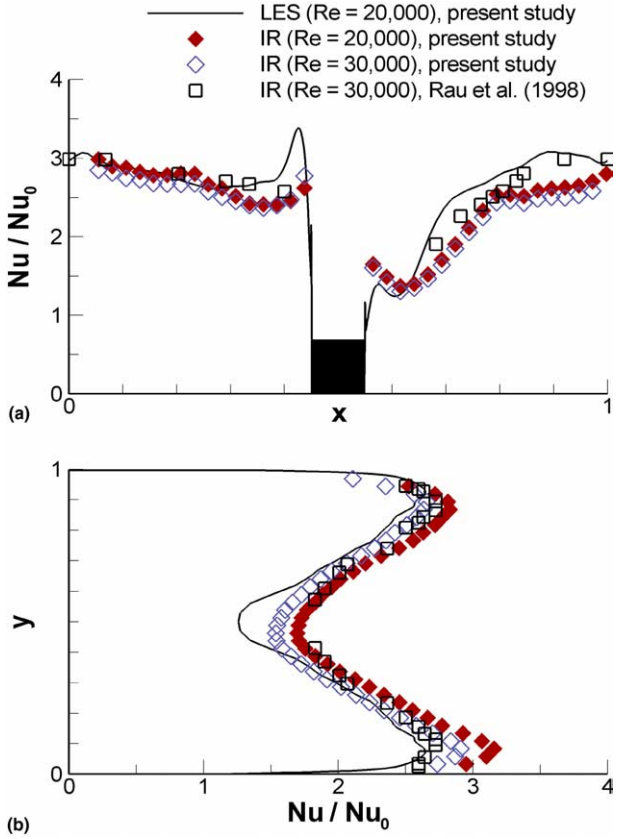

Fig. 14. Comparisons between the heat transfer calculations and experiments of Rau et al. (1998) on (a) the centerline of the ribbed wall and (b) a vertical line on the smooth side wall upstream of the rib show excellent agreement between experiments and calculations.

fer augmentation develops very quickly in the developing flow region (Han and Park, 1988; Liou and Hwang, 1992a; Sewall and Tafti, 2004a).

Heat transfer studies in the fully developed section are common and are typically used for validation of numerical calculations. Two common comparisons of heat transfer measurements were reported by Rau et al. (1998), which show experimental measurements for a case very similar to the present one ($e/D_h = 0.1$, $P/e = 9$) but with a Reynolds number of 30,000. One is a line along the centerline of the ribbed wall, and the other is a vertical line on the smooth wall that is one rib height upstream of the centerline of the rib. The infrared camera measurements for $Re = 20{,}000$ and $Re = 30{,}000$ are shown along with the measurements of Rau et al. for those two locations in Fig. 14. The values are shown to compare very well. On the ribbed wall, the calculation shows a region of high heat transfer augmentation upstream of the rib, and this region is either too small for observation or lost in the shadow of the rib in the measurements. In Fig. 14(b), the agreement with the measurements is good, also. The high heat transfer shown near the ribbed walls is a consequence of the secondary flows pictured in Fig. 9, which increases the heat transfer due to lateral flow impingement upstream of the rib. In the channel center, the heat transfer is slightly under-

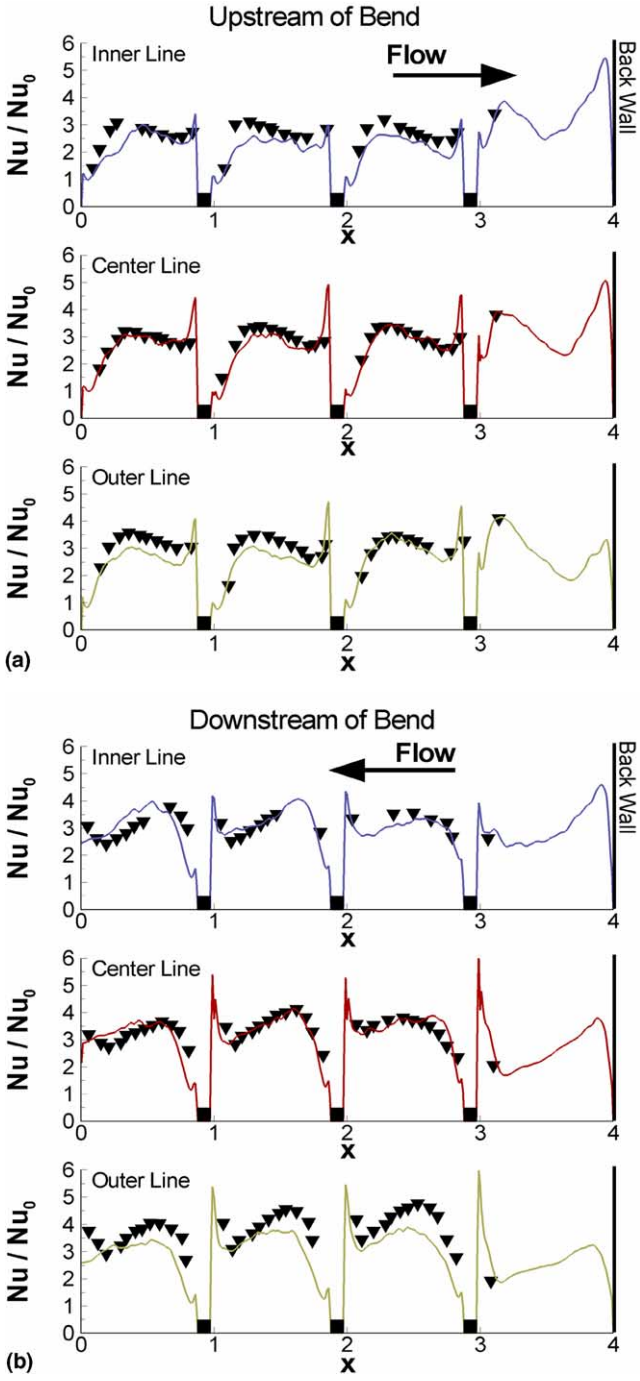

Fig. 15. Comparisons of heat transfer augmentation between the LES calculation and the mass transfer experiments of Han et al. (1988) along the inner line, center line, and outer line of (a) the region upstream of the bend and (b) the region downstream of the bend show the good agreement between the calculations and experiments.

predicted, but the overall comparison is very good. The accurate prediction of these two curves is difficult to achieve because of the recirculation of flow near the ribs and the localized secondary flow effect. Many computational studies have attempted to correctly predict this smooth wall heat transfer effect using different turbulence models with little success (Ooi et al., 2002; Arts et al., 1997; Saidi and Sundén, 2001; Sleiti and Kapat, 2004).

In the 180° bend region, a mass transfer experiment by Han et al. (1988) showed results for a channel with geometry similar to that of the present study ($e/D_h = 0.094$, $P/e = 10$) with a Reynolds number of 30,000. No rib is included in the bend in either case. One difference between the two studies is the width of the dividing wall between the upstream and downstream ducts, which is $1/4D_h$ in the experiments and $1/2D_h$ in the calculations. This parameter has an important effect on the flow and heat transfer characteristics, as was shown in a smooth wall 180° bend study by Liou et al. (1999). Comparisons between six lines on the ribbed walls are shown in Fig. 15. The lines are local mass transfer measurements along three lines in each leg of the bend. One line is along the center, one is between the center and inside wall (''inner line''), and the other is between the center and outside wall (''outer line''). Comparisons upstream of the bend are shown in Fig. 15(a), and comparisons downstream of the bend are shown in Fig. 15(b). Agreement between the experiments and comparisons upstream of the bend is very good. The magnitudes of the inner, center, and outer lines do not vary much, indicating that the bend has very little effect on the flow upstream. Downstream, the measured heat transfer is higher coming out of the bend on the outer line than the predictions show, but this is expected because the thinner dividing wall in the experiments induces a stronger flow separation, increasing the heat transfer along the outside line. Careful study of the heat transfer magnitudes shows that the bend has a strong influence on increasing the heat transfer augmentation downstream, which is a positive result produced by the presence of the bend.

6. Conclusion

Modeling ribbed duct flows is a significant challenge facing the gas turbine industry. The current industry standard is to use RANS simulations with a variety of turbulence models. These techniques are relied upon heavily mostly because of their ease of use and fast turnaround time in obtaining results. However, the models seldom accurately reproduce the range of physics encountered in internal cooling ducts. The present study validates the use of LES for predicting flow and heat transfer with experiments and elucidates on the detailed physics encountered in the developing flow region, the fully developed region, and the 180° bend region.

The results show that the heat transfer is augmented over that of a smooth duct by a factor between 2 and 3. The friction is augmented by a factor of 10, primarily due to form losses from the ribs. The primary mechanism of heat transfer augmentation is the generation of unsteady vortical structures in separated shear layers on ribs and at rib junctions with the ribbed and smooth walls. The unsteady vorticity, which continuously replenishes and mixes fluid in wall boundary layers, manifests itself in the mean as increased turbulent intensities in boundary layers. While secondary flows in the duct cross-section and the 180° bend have a large impact on heat transfer, they do not have as large an impact on frictional losses, which are dominated by form losses.

Among the major flow features predicted with accuracy are shear layer transition at the entrance of the duct; the distribution of mean and turbulent quantities in the developing, fully developed, and 180° bend; the development of secondary flows in the duct cross-section and the 180° bend; and friction and heat transfer augmentation. In all different aspects, it is found that LES produces the correct physics both qualitatively and quantitatively to within 10–15%.

Acknowledgements

This research was supported by the US DOE, Office of Fossil Energy, National Energy Technology Laboratory. Any opinions, findings, conclusions, or recommendations expressed herein are those of the author and do not necessarily reflect the views of the DOE. This work was also supported by National Computational Science Alliance under MCA98N042N and utilized the Titan and Teragrid Linux clusters at the National Center for Supercomputing Applications.

The authors would also like to thank Sara P. Borka for her work on the heat transfer measurements.

References

Abdel-Wahab, S., Tafti, D.K., 2004a. Large eddy simulation of flow and heat transfer in a 90° ribbed duct with rotation: effect of Coriolis and centrifugal buoyancy forces. ASME Journal of Turbomachinery 126, 627–636.

Abdel-Wahab, S., Tafti, D.K., 2004b. Large eddy simulation of flow and heat transfer in a staggered 45° ribbed duct. In: Proceedings of the ASME Turbo Expo 2004, Vienna, Austria, ASME Paper No. GT2004-53800.

Acharya, S., Dutta, S., Myrum, T.A., Baker, R.S., 1993. Periodically developed flow and heat transfer in a ribbed duct. International Journal of Heat and Mass Transfer 36 (8), 2069–2082.

Al-Qahtani, M., Jang, Y.-J., Chen, H.-C., Han, J.-C., 2002a. Prediction of flow and heat transfer in rotating two-pass rectangular channels with 45-deg rib turbulators. ASME Journal of Turbomachinery 124, 242–250.

Al-Qahtani, M., Chen, H.-C., Han, J.-C., 2002b. A numerical study of flow and heat transfer in rotating rectangular channels (AR = 4) with 45° rib turbulators by Reynolds stress turbulence model. In: Proceedings of the ASME Turbo Expo 2002, Amsterdam, The Netherlands, ASME Paper No. GT-2002-30216.

Arts, T., Rau, G., Çakan, M., Vialonga, J., Fernandez, D., Tarnowski, F., Laroche, E., 1997. Experimental and numerical investigation on flow and heat transfer in large-scale, turbine cooling, representative, rib-roughened channels. In: Proceedings of the Institution of Mechanical Engineers (ImechE) 211 (Part A), 263–272.

Astarita, T., Cardone, G., 2003. Convective heat transfer in a square channel with angled ribs on two opposite walls. Experiments in Fluids 34, 625–634.

Astarita, T., Cardone, G., Carlomagno, G.M., 2002. Convective heat transfer in ribbed channels with a 180° turn. Experiments in Fluids 33, 90–100.

Baughn, J.W., Yan, X., 1992. Local heat transfer measurements in square ducts with transverse ribs. ASME HTD, Enhanced Heat Transfer 202, 1–7.

Besserman, D.L., Tanrikut, S., 1992. Comparison of heat transfer measurements with computations for turbulent flow around a 180 deg bend. ASME Journal of Turbomachinery 114, 865–871.

Bonhoff, B., Tomm, U., Johnson, B.V., Jennions, I., 1997. Heat transfer predictions for rotating u-shaped coolant channels with skewed ribs and with smooth walls. In: Proceedings of the International Gas Turbine & Aeroengine Congress & Exhibition, Orlando, Florida, USA, Paper No. 97-GT-162.

Bonhoff, B., Parneix, S., Leusch, J., Johnson, B.V., Schabacker, J., Bölcs, A., 1999. Experimental and numerical study of developed flow and heat transfer in coolant channels with 45 degree ribs. International Journal of Heat and Fluid Flow 20, 311–319.

Chang, S.W., Morris, W.D., 2003. Heat transfer in a radially rotating square duct fitted with in-line transverse ribs. International Journal of Thermal Sciences 42, 267–282.

Chen, Y., Nikitopoulos, D.E., Hibbs, R., Acharya, S., Myrum, T.A., 2000. Detailed mass transfer distribution in a ribbed coolant passage with a 180° bend. International Journal of Heat and Mass Transfer 43, 1479–1492.

Durst, F., Founti, M., Obi, S., 1988. Experimental and computational investigation of the two-dimensional channel flow over two fences in tandem. ASME Journal of Fluids Engineering 110, 48–54.

Ekkad, S.V., Pamula, G., Shantiniketanam, M., 2000. Detailed heat transfer measurements inside straight and tapered two-pass channels with rib turbulators. Experimental Thermal and Fluid Science 22, 155–163.

Fann, S., Yang, W.-J., Zhang, N., 1994. Local heat transfer in a rotating serpentine passage with rib-roughened surfaces. International Journal of Heat and Mass Transfer 37 (2), 217–228.

Germano, M., Piomelli, U., Moin, P., Cabot, W.H., 1991. A dynamic subgrid-scale eddy viscosity model. Physics of Fluids A 3, 1760–1765.

Graham, A., Sewall, E., Thole, K.A., 2004. Flowfield measurements in a ribbed channel relevant to internal turbine blade cooling. In: Proceedings of the ASME Turbo Expo 2004, Vienna, Austria, ASME Paper No. GT2004-53361.

Gu, X., Wu, H.-W., Schock, H.J., Shih, T.I.-P., 2002. Two-equation Versus Reynolds-stress modeling in predicting flow and heat transfer in a smooth U-duct with and without rotation. In: Proceedings of the ASME Turbo Expo 2002, Amsterdam, The Netherlands, ASME Paper No. GT-2002-30616.

Han, J.C., 1984. Heat transfer and friction in channels with two opposite rib-roughened walls. ASME Journal of Heat Transfer 106, 774–781.

Han, J.C., Park, J.S., 1988. Developing heat transfer in rectangular channels with rib turbulators. International Journal of Heat and Mass Transfer 31 (1), 183–195.

Han, J.C., Chandra, P.R., Lau, S.C., 1988. Local heat/mass transfer distributions around sharp 180 deg turns in two-pass smooth and rib-roughened channels. ASME Journal of Heat Transfer 110, 91–98.

Hirota, M., Yokosawa, H., Fujita, H., 1992. Turbulence kinetic energy in turbulent flows through square ducts with rib-roughened walls. International Journal of Heat and Fluid Flow 13 (1), 22–29.

Iacovides, H., Raisee, M., 2001. Computation of flow and heat transfer in two-dimensional rib-roughened passages, using low-Reynolds-number turbulence models. International Journal of Numerical Methods for Heat & Fluid Flow 11 (2), 138–155.

Iacovides, H., Kelemenis, G., Raisee, M., 2003. Flow and heat transfer in straight cooling passages with inclined ribs on opposite walls: an experimental and computational study. Experimental Thermal and Fluid Science 27, 283–294.

Incropera, F.P., DeWitt, D.P., 2002. Fundamentals of Heat and Mass Transfer, fifth ed. John Wiley & Sons, New York.

Islam, M.S., Haga, K., Kaminaga, M., Hino, R., Monde, M., 2002. Experimental analysis of turbulent flow structure in a fully developed rib-roughened rectangular channel with PIV. Experiments in Fluids 33, 296–306.

Jang, Y.-J., Chen, H.-C., Han, J.-C., 2001. Flow and heat transfer in a rotating square channel with 45 deg angled ribs by Reynolds stress turbulence model. ASME Journal of Turbomachinery 123, 124–132.

Jia, R., Saidi, A., Sundén, B., 2002. Heat transfer enhancement in square ducts with V-shaped ribs of various angles. In: Proceedings of the ASME Turbo Expo 2002, Amsterdam, The Netherlands, ASME Paper No. GT-2002-30209.

Lilly, D.K., 1992. A proposed modification of the Germano subgrid-scale eddy viscosity model. Physics of Fluids A 4 (3), 633–635.

Lin, Y.-L., Shih, T.I.-P., Stephens, M.A., Chyu, M.K., 2001. A numerical study of flow and heat transfer in a smooth and ribbed U-duct with and without rotation. ASME Journal of Heat Transfer 123, 219–232.

Liou, T.-M., Hwang, J.-J., 1992a. Developing heat transfer and friction in a ribbed rectangular duct with flow separation at inlet. ASME Journal of Heat Transfer 114, 565–573.

Liou, T.-M., Hwang, J.-J., 1992b. Turbulent Heat Transfer Augmentation and Friction in Periodic Fully Developed Channel Flows. ASME Journal of Heat Transfer 114, 56–64.

Liou, T.-M., Chang, Y., Hwang, D.-W., 1990. Experimental and computational study of turbulent flows in a channel with two pairs of turbulence promoters in tandem. ASME Journal of Fluids Engineering 112, 302–310.

Liou, T.-M., Hwang, J.-J., Chen, S.-H., 1992. Turbulent transport phenomena in a channel with periodic rib turbulators. Journal of Thermophysics and Heat Transfer 6 (3), 513–521.

Liou, T.-M., Wu, Y.-Y., Chang, Y., 1993a. LDV measurements of periodic fully developed main and secondary flows in a channel with rib-disturbed walls. ASME Journal of Fluids Engineering 115, 109–114.

Liou, T.-M., Hwang, J.-J., Chen, S.-H., 1993b. Simulation and measurement of enhanced turbulent heat transfer in a channel with periodic ribs on one principal wall. International Journal of Heat and Mass Transfer 36 (2), 507–517.

Liou, T.-M., Tzeng, Y.-Y., Chen, C.-C., 1999. Fluid flow in a 180 deg sharp turning duct with different divider thicknesses. ASME Journal of Turbomachinery 121, 569–576.

Mochizuki, S., Murata, A., Shibata, R., Yang, W.-J., 1999. Detailed measurements of local heat transfer coefficients in turbulent flow through smooth and rib-roughened serpentine passages with a 180° sharp bend. International Journal of Heat and Mass Transfer 42, 1925–1934.

Moffat, R.J., 1988. Describing the uncertainties in experimental results. Experimental Thermal Fluid Science 1, 3–17.

Murata, A., Mochizuki, S., 2001. Comparison between laminar and turbulent heat transfer in a stationary square duct with transverse or angled rib turbulators. International Journal of Heat and Mass Transfer 44, 1127–1141.

Ooi, A., Iaccarino, G., Durbin, P.A., Behnia, M., 2002. Reynolds averaged simulation of flow and heat transfer in ribbed ducts. International Journal of Heat and Fluid Flow 23, 750–757.

Park, C.W., Lau, S.C., Kukreja, R.T., 1998. Heat/mass transfer in a rotating two-pass channel with transverse ribs. Journal of Thermophysics and Heat Transfer 12 (1), 80–86.

Prakash, C., Zerkle, R., 1995. Prediction of turbulent flow and heat transfer in a ribbed rectangular duct with and without rotation. ASME Journal of Turbomachinery 117, 255–264.

Rau, G., Çakan, M., Moeller, D., Arts, T., 1998. The effect of periodic ribs on the local aerodynamic and heat transfer performance of a straight cooling channel. ASME Journal of Turbomachinery 120, 368–375.

Saha, A.K., Acharya, S., 2003. Flow and heat transfer in an internally ribbed duct with rotation: an assessment of LES and URANS. In: Proceedings of the ASME Turbo Expo 2003, Atlanta, Georgia, USA, ASME Paper No. GT2003-38619.

Saidi, A., Sundén, B., 2001. On prediction of thermal-hydraulic characteristics of square-sectioned ribbed cooling ducts. ASME Journal of Turbomachinery 123, 614–620.

Sato, H., Hishida, K., Maeda, M., 1989. Turbulent flow characteristics in a rectangular channel with repeated rib roughness. ASME HTD, Heat Transfer in Convective Flows 107, 191–196.

Schabacker, J., Bölcs, B.V., Johnson, B.V., 1998. PIV investigation of the flow characteristics in an internal coolant passage with two ducts connected by a sharp 180° bend. In: Proceedings of the International

Gas Turbine & Aeroengine Congress & Exhibition, Stockholm, Sweden, ASME Paper No. 98-GT-544.

Sewall, E.A., Tafti, D.K., 2004a. Large eddy simulation of the developing region of a stationary ribbed internal turbine blade cooling channel. In: Proceedings of the ASME Turbo Expo 2004, Vienna, Austria, ASME Paper No. GT2004-53832.

Sewall, E.A., Tafti, D.K., 2004b. Large eddy simulation of the developing region of a rotating ribbed internal turbine blade cooling channel. In: Proceedings of the ASME Turbo Expo 2004, Vienna, Austria, ASME Paper No. GT2004-53833.

Shih, T.I.-P., Lin, Y.-L., Stephens, M.A., Chyu, M.K., 1998. Flow and heat transfer in a ribbed U-duct under typical engine conditions. In: Proceedings of the International Gas Turbine & Aeroengine Congress & Exhibition, Stockholm, Sweden, Paper No. 98-GT-213.

Sleiti, A.K., Kapat, J.S., 2004. Comparison between EVM and RSM turbulence models in predicting flow and heat transfer in rib-roughened channels. In: Proceedings of the 2004 ASME Heat Transfer/Fluids Engineering Summer Conference, Charlotte, North Carolina, USA, ASME Paper No. HT-FED04-56250.

Son, S.Y., Kihm, K.D., Han, J.-C., 2002. PIV flow measurements for heat transfer characterization on two-pass square channels with smooth and 90° ribbed walls. International Journal of Heat and Mass Transfer 45, 4809–4822.

Tafti, D.K., 2001. GenIDLEST—a scalable parallel computational tool for simulating complex turbulent flows. In: Proceedings of the ASME Fluids Engineering Division, FED, vol. 256. ASME-IMECE, New York.

Tafti, D.K., 2005. Evaluating the role of subgrid stress modeling in a ribbed duct for the internal cooling of turbine blades. International Journal of Heat and Fluid Flow 26, 92–104.

Wagner, J.H., Johnson, B.V., Graziani, R.A., Yeh, F.C., 1992. Heat transfer in rotating serpentine passages with trips normal to the flow. ASME Journal of Turbomachinery 114, 847–857.

Wang, L.-B., Tao, W.-Q., Wang, Q.-W., Wong, T.T., 2001. Experimental study of developing turbulent flow and heat transfer in ribbed convergent/divergent square ducts. International Journal of Heat and Fluid Flow 22, 603–613.

Watanabe, K., Takahashi, T., 2002. LES simulation and experimental measurement of fully developed ribbed channel flow and heat transfer. In: Proceedings of the ASME Turbo Expo 2002, Amsterdam, The Netherlands, ASME Paper No. GT-2002-30203.

Zhao, C.Y., Tao, W.Q., 1997. A three dimensional investigation of turbulent flow and heat transfer around sharp 180-deg turns in two-pass rib-roughened channels. International Communications in Heat and Mass Transfer 24 (4), 587–596.